



Geophysical Research Letters*



RESEARCH LETTER

10.1029/2023GL103692

Key Points:

- Mobile X-band polarimetric radar Range Height Indictor scans were directly collocated with overpassing multi-frequency airborne radars during a snowstorm
- Three separate mass-weighted mean diameter retrievals had mean absolute errors of 0.49, 0.74, and 0.93 mm between each other
- These results provide a one-of-a-kind, high-resolution benchmark for comparing retrieval methods across various platforms

Correspondence to:

E. L. Dunnavan, edwin.dunnavan@noaa.gov

Citation:

Dunnavan, E. L., Carlin, J. T., Schvartzman, D., Ryzhkov, A. V., Bluestein, H., Emmerson, S., et al. (2023). High-resolution snowstorm measurements and retrievals using cross-platform multi-frequency and polarimetric radars. *Geophysical Research Letters*, 50, e2023GL103692. https://doi.org/10.1029/2023GL103692

Received 14 MAR 2023 Accepted 14 JUN 2023

© 2023. The Authors.

This is an open access article under the terms of the Creative Commons Attribution License, which permits use, distribution and reproduction in any medium, provided the original work is properly cited.

High-Resolution Snowstorm Measurements and Retrievals Using Cross-Platform Multi-Frequency and Polarimetric Radars

Edwin L. Dunnavan^{1,2}, Jacob T. Carlin^{1,2}, David Schvartzman^{3,4}, Alexander V. Ryzhkov^{1,2}, Howard Bluestein³, Samuel Emmerson^{3,4}, Greg M. McFarquhar^{1,3}, Gerald M. Heymsfield⁵, and John Yorks⁵

¹Cooperative Institute for Severe and High-Impact Weather Research and Operations, University of Oklahoma, Norman, OK, USA, ²NOAA/OAR National Severe Storms Laboratory, Norman, OK, USA, ³School of Meteorology, University of Oklahoma, Norman, OK, USA, ⁴Advanced Radar Research Center, University of Oklahoma, Norman, OK, USA, ⁵NASA Goddard Space Flight Center, Greenbelt, MD, USA

Abstract Many studies have performed microphysical retrievals using radars of different frequencies, platforms, and methodologies. However, little is known about the consistency of retrievals derived from different radar platforms (i.e., airborne or spaceborne vs. ground-based) and their methodologies. This study is the first to directly compare snow mass-weighted mean diameter (D_m) retrievals from both nadir-pointing airborne multi-frequency radars and ground-based polarimetric range-height indicator radar scans along the same airborne flight track with a resolution of $\mathcal{O}(10 \text{ m})$. D_m retrievals between each method produced mean absolute errors of 0.49, 0.74, and 0.93 mm where the largest differences were between the ground and aircraft retrievals. A triple-frequency analysis suggests the possibility that snow aggregates were generally composed of needles. These results can be used as a benchmark for comparing retrieval methodologies and highlight the continued uncertainty regarding the optimal approach for ice microphysical retrievals.

Plain Language Summary Both airborne and ground-based weather radar measurements can be used to estimate snowflake characteristics such as their mean size. However, it is difficult to compare the radar-estimated mean sizes between these platforms because of the vast methodological differences in how these sizes are estimated and the spatial and temporal differences resulting from each radar's geographical location. This study is the first to directly compare snowflake size retrievals using ground-based mobile radar scans that collected data along the same path as an overhead-passing aircraft, thus directly minimizing any error resulting from matching values between radars aboard the aircraft and the ground radar. We also used the aircraft radars' multiple frequencies to investigate what types of particles were dominant throughout the storm. Through this multi-frequency analysis, we found that it is possible that snow particles were aggregates of thin needles that were stuck together. These results can be used by other researchers and forecasters to understand how snowflake size estimates can vary between different platforms and methodologies.

1. Introduction

Weather radars are among the most important meteorological tools available to observe large-scale microphysical and macrophysical precipitation characteristics. Typically, radars have been used to estimate, or retrieve, a number of key ice microphysical parameters including ice water content (IWC) (Chase et al., 2021; Dunnavan et al., 2022; Murphy et al., 2020; Ryzhkov et al., 1998), precipitation rate (Bukovčić et al., 2018, 2020; Le & Chandrasekar, 2019; Skofronick-Jackson et al., 2019), particle shape (Matrosov et al., 2017; Myagkov et al., 2016), number concentration (N_t), mean volume diameter (D_{mv}) (Dunnavan et al., 2022; Murphy et al., 2020), and mass-weighted mean diameter (D_m) (Chase et al., 2020). The accuracy and fidelity of these retrievals are contingent upon a number of factors including the platform on which the radar operates (i.e., ground-based, airborne, or spaceborne), the radar frequency, the variables used, and the underlying physical assumptions.

Because of the additional independent information they provide, multi-parameter radar measurements are well-suited for performing retrievals by constraining microphysical uncertainty. The two primary multi-parameter retrieval approaches use either multi-frequency or dual-polarization radar measurements. Multi-frequency retrievals of microphysical variables such as D_{mv} and D_m capitalize on different scattering regimes between

DUNNAVAN ET AL. 1 of 11

9448007, 2023, 12, Downloaded from https:/

frequencies and have been shown to have utility (Liao et al., 1997, 2005; Matrosov, 1992), with state-of-theart methods yielding average root mean square errors of 0.8–1.0 mm with respect to in-situ aircraft measurements (Chase et al., 2021; Matrosov et al., 2022). However, with the exception of a few long-term ground-based multi-frequency data collection sites (e.g., Kollias et al., 2020; Löhnert et al., 2015; National Centre for Atmospheric Science, 2023), most ground-based and airborne multi-frequency data sets have thus far been limited to specific research field campaigns (e.g., Dias Neto et al., 2019; Nguyen et al., 2022; Petäjä et al., 2016). Similarly, continuously operating multi-frequency spaceborne platforms with global coverage [e.g., the Global Precipitation Mission's Dual-frequency Precipitation Radar (GPM–DPR)] have limited vertical resolution.

Polarimetric retrieval methods of D_{mv} (Dunnavan et al., 2022; Ryzhkov & Zrnić, 2019) have received increasing attention and are operationally viable given the ubiquitous nature of available ground-based polarimetric radars such as the NEXRAD network (Zrnić & Ryzhkov, 1999). However, polarimetric variables such as specific differential phase ($K_{\rm dp}$) require spatial averaging to accurately compute, and all multi-parameter approaches rely to varying degrees on uncertain assumptions regarding the microphysical characteristics of the ice particles and their size distributions. Due to the difficulty of spatially and temporally collocating data from different platforms and the inability to meaningfully utilize polarimetric variables from nadir- and zenith-pointing platforms, we are unaware of any existing multi-frequency and polarimetric microphysical retrieval comparisons. While some spatiotemporal uncertainties in matching retrievals from different platforms can be quantified with statistical methods such as bootstrap sampling (Dunnavan et al., 2022), it can be difficult to quantify the intrinsic consistency and accuracy among various retrieval methodologies. As a result, there is a strong need for a reliable benchmark to aid in reporting the performance of different retrieval methodologies from various platforms and how consistent they are with one another.

This study is unique in that we utilize high-resolution airborne radars and coincident ground-based Range Height Indicator (RHI) scans *along* an aircraft flight track. This allows us to provide a much better comparison of cross-platform radar retrieval performance that is more than two orders of magnitude higher resolution than even the most advanced and current inter-platform retrieval studies such as Skofronick-Jackson et al. (2019) and Chase et al. (2021). For simplicity, we focus on retrieving only one microphysical quantity: D_m . By evaluating the statistics of coincident multi-frequency and dual-polarization D_m retrievals over entire range and height profiles, we are able to assess the consistency of retrievals between each platform and method with much higher spatial $[\mathcal{O}(10 \text{ m})]$ and temporal $[\mathcal{O}(1 \text{ s})]$ resolutions than other evaluation efforts.

2. Case Overview and Methodology

On 25 February 2022, the NASA-led Investigation of Microphysics and Precipitation for Atlantic Coast-Threatening Snowstorms (IMPACTS) field campaign (McMurdie et al., 2022) conducted an intensive observation period (IOP) in upstate New York with a variety of instrumentation. This snowstorm was a part of a large warm frontal system that passed through the northeast United States. The NASA ER-2 aircraft performed north—south and south—north passes over the Advanced Radar Research Center's (ARRC) Rapid-scanning X-band Polarimetric (RaXPol) mobile radar (Pazmany et al., 2013) stationed in Albany, New York (Figure 1). Each overpass came within ≈100 m of RaXPol, with five overpasses coming within 50 m. The ER-2 aircraft housed a number of nadir-pointing radars including the X-band EXRAD radar (9.6 GHz; Heymsfield et al., 2020), the W-band CRS radar (94 GHz; McLinden et al., 2020), and the Ku- (13.91 GHz) and Ka-band (35.56 GHz) radars from the HIWRAP instrument (Li et al., 2020). Ground instruments including a zenith-pointing Micro Rain Radar 2 (MRR-2) and a Parsivel² disdrometer (Löffler-Mang & Joss, 2000) were located in the Emerging Technology & Entrepreneurship Complex (ETEC) building yard of the State University of New York at Albany (SUNY Albany), just 0.8 km northwest of RaXPol as shown in Figure 1.

Figure 2 shows the MRR-2 measurements of reflectivity Z, mean Doppler velocity (MDV), and spectral width from the nearby ETEC yard (Figure 1) for the times of these overpasses. The ER-2 aircraft performed a total of 10 overpasses (shown as colored, shaded bars on Figure 2) directly above the RaXPol radar. Each overpass period denotes when the ER-2 was within ± 45 km of RaXPol along its flight line. Of these 10 overpass periods, 8 were during periods when the RaXPol was collecting $0-90^\circ$ RHIs (green bars). For six of these periods, synthetic full-hemispheric RHIs were reconstructed by compositing successive RHI scans closest in time to the overpass in either direction. Throughout most of the event, the precipitation structure was fairly smooth and consistent with time, with clear and gradual increases of Z and MDV toward the surface likely indicative of aggregation

DUNNAVAN ET AL. 2 of 11

9448007, 2023, 12, Downloaded from https://agupubs.onlinelibrary.wiley.com/doi/10.1029/2023GL103692, Wiley Online Library on [23/07/2023]. See the Terms

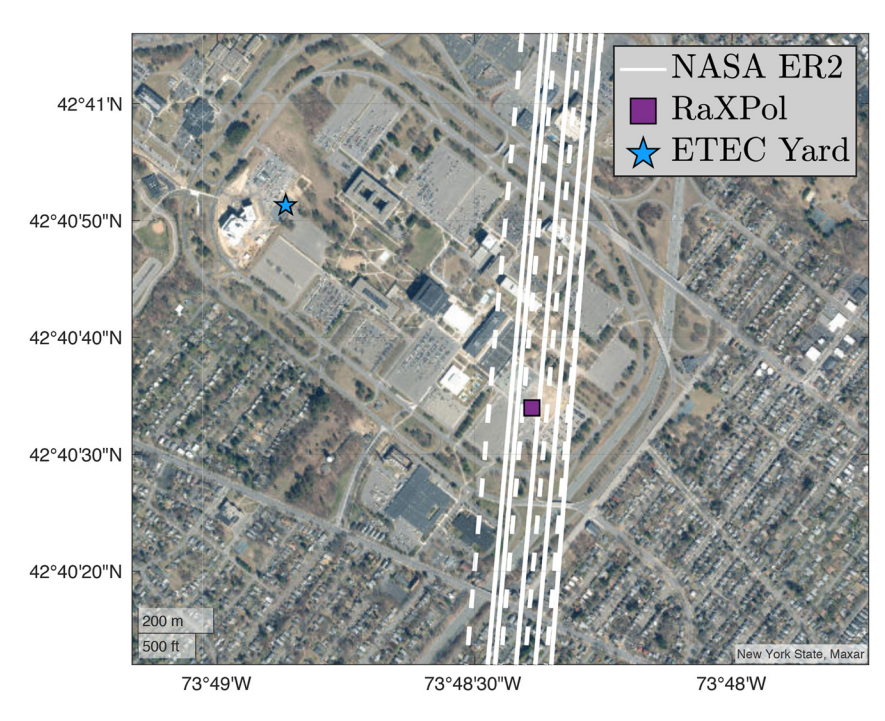


Figure 1. NASA ER-2 aircraft flight track overpasses with the locations of RaXPol and the SUNY Albany ETEC Yard. The satellite image is from the New York State Maxar (Copyright Maxar). Solid lines indicate N-S passes and dashed lines indicate S-N passes.

(Schrom & Kumjian, 2016). Toward the last of the overpass periods, the Z field becomes more sporadic, with more discrete and transient fallstreaks and an increase in the magnitude of the MDV and spectral width enhancements around 2.0 km MSL. The spectral width enhancement coincides with a region of enhanced saturation, thus indicating likely vapor growth and the possibility of riming at temperatures of about -5°C .

We performed a number of corrections and calibration adjustments to both the ER-2 and RaXPol radar data. First, radar variables from both platforms were linearly interpolated onto a common 50 m × 50 m Cartesian grid. Next, attenuation correction following Finlon et al. (2022) was implemented. The International Telecommunication Union (2013) recommendations were used to correct the RaXPol data and all four frequencies of the ER-2 data for gaseous attenuation. Next, the methodology of Meneghini and Kozu (1990) was used to correct the ER-2 W-, Ka-, and Ku-band data for attenuation due to supercooled liquid water using the High-Resolution Rapid Refresh (HRRR) model (Benjamin et al., 2016) analysis profiles nearest in time and space to RaXPol's location; attenuation due to supercooled liquid water was assumed to be negligible for the ER-2 and RaXPol X-band data. Additional attenuation correction was performed for ice absorption for the CRS W-band data using the mean Z_{Ku} —W-band specific attenuation (A_{W}) relation of Kulie et al. (2014) (their Figure 7). Note that W-band attenuation due to ice absorption can be appreciable, and its correction remains a source of uncertainty due to its sensitivity to the assumed ice particle characteristics (Tridon et al., 2019); prior work addressing this issue has ranged from neglecting it entirely to finding $A_{\rm W}$ rates of up to 4 dB km⁻¹ (Protat et al., 2019). Once the attenuation correction was complete, absolute calibration was performed for each overpass and frequency. The HIWRAP Ku-band $Z(Z_{Ku})$ served as our reference profile for the other airborne radar data as it undergoes minimal attenuation and is believed to be the best calibrated due to the legacy of Ku-band calibration from TRMM (Kummerow et al., 1998) and the GPM-DPR. The mean EXRAD X-band (CRS W-band) Z offset was found by comparing regions where $10 < Z_{\rm Ku} < 20~{\rm dBZ}$ (5 $< Z_{\rm Ku} < 15~{\rm dBZ}$) between 4.5 and 5.5 km (6.5–7.5 km) MSL, with overall mean offsets from $Z_{K_{II}}$ of +4.08 and -0.74 dB, respectively. The HIWRAP Ka-band radar was found to have a constant offset of +0.77 dB. This approach resulted in ≈0 dB DWRs between the various radar frequencies for the Rayleigh ice scatterers at cloud top, with differences growing downward between contiguous radar bands due to attenuation and non-Rayleigh scattering in accordance with theoretical expectations. The RaXPol Z was calibrated against the adjusted EXRAD X-band data using the mean difference at zenith between 0 and 7 km MSL at each time; a mean adjustment of -6.25 dB was determined. RaXPol $K_{\rm dp}$ was calculated using the Py-ART

DUNNAVAN ET AL. 3 of 11

19448007, 2023, 12, Downloaded from https://agupubs.onlinelibrary.wiley.com/doi/10.1029/2023GL103692, Wiley Online Library on [23/07/2023]. See the Terms and Conditions (https://onlinelibrary.wiley.com/erms-and-conditions) on Wiley Online Library for rules of use; OA articles are governed by the applicable Creat

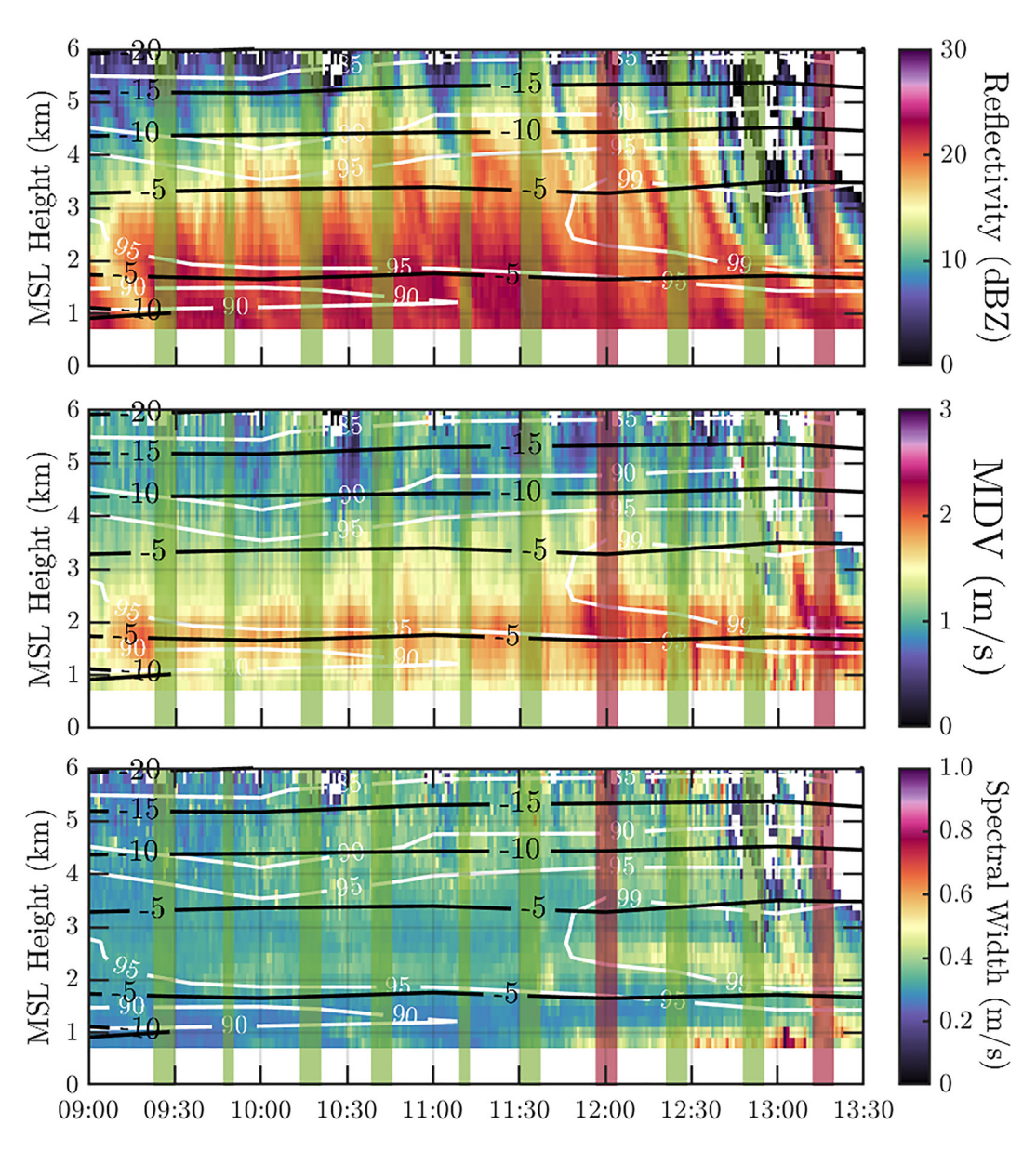


Figure 2. MRR-2 timeseries (UTC) of *Z* (top), mean Doppler velocity (middle), and spectral width of the most significant peak (bottom). Green bars represent periods of ER-2 flyover coincident (i.e., within 45 km, horizontal) with the RaXPol. Red bars indicate flyover periods when RaXPol was not scanning Range Height Indictors. Contours of temperature (black contours; °C) and relative humidity with respect to liquid water (white contours; %) from the HRRR model are also shown.

(Helmus & Collis, 2016) implementation of the Vulpiani et al. (2012, 2015) method with a 10-gate window and 11 iterations and was limited to regions with signal-to-noise ratios (SNR) greater than 7 dB (e.g., Schvartzman et al., 2020). The $K_{\rm dp}$ was corrected for elevation angle (θ) by dividing $K_{\rm dp}$ by $\cos^2(\theta)$ (Ryzhkov & Zrnić, 2019). Only the lowest 45° of RaXPol's elevation angles are used to eliminate large errors in the $K_{\rm dp}$ correction that stem from a singularity as θ approaches 90°. The computed $K_{\rm dp}$ was similarly interpolated onto a matching Cartesian grid.

Figure 3 shows example comparisons between the ER-2 and RaXPol measurements for three of the overpasses. With the calibration adjustments made to each radar, the ER-2 EXRAD and RaXPol X-band reflectivities provide a nearly visually identical field for two of these overpass events (0926 UTC and 1251 UTC) whereas 1042 UTC shows slightly lower RaXPol Z values than the ER-2 EXRAD. In particular, both the ER-2 EXRAD and RaXPol radars are able to capture the same sub-kilometer Z features such as the layered precipitation apparent at 1042 UTC and the discrete fallstreak features at 1251 UTC which appear in Figure 2. Other variables, such as the

DUNNAVAN ET AL. 4 of 11

1944/8007, 2023, 12, Downloaded from https://augupubs.onlinelibrary.wiley.com/doi/10.1029/2023GL103692, Wiley Online Library on [23/07/2023]. See the Terms and Conditions (https://onlinelibrary.wiley.com/terms-and-conditions) on Wiley Online Library for rules of use; OA articles are governed by the applicable Creative Creative Creative Conditions (https://onlinelibrary.wiley.com/terms-and-conditions) on Wiley Online Library for rules of use; OA articles are governed by the applicable Creative Creative Creative Creative Conditions (https://onlinelibrary.wiley.com/terms-and-conditions) on Wiley Online Library for rules of use; OA articles are governed by the applicable Creative Cr

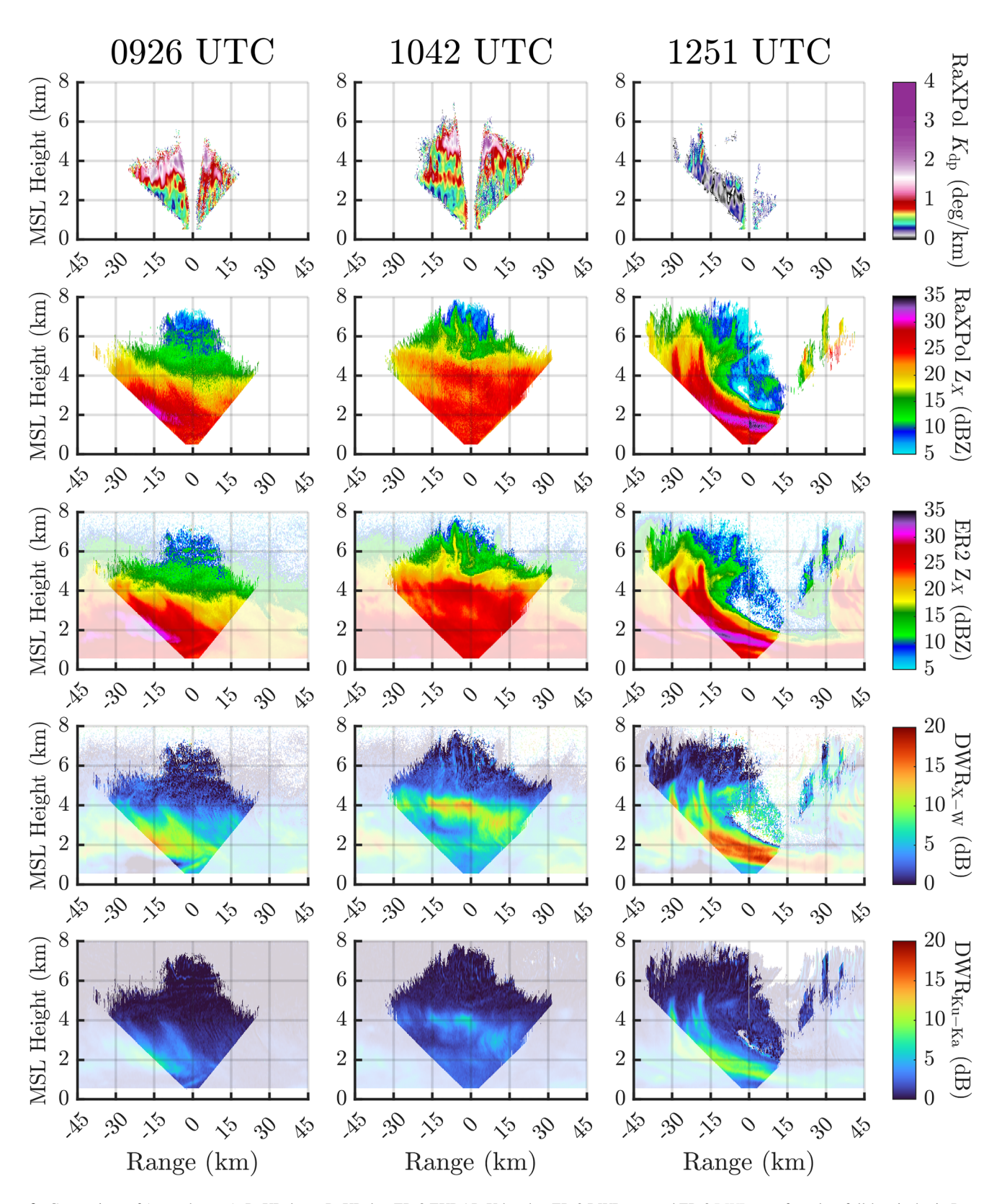


Figure 3. Comparison of (top to bottom): RaXPol K_{dp} , RaXPol Z, ER-2 EXRAD X-band Z, ER-2 DWR_{X-W}, and ER-2 DWR_{K_u-K_u} for select full-hemispheric-Range Height Indictor (RHI) overpass events of the RaXPol. Transparencies in the ER-2 plots are used to highlight the outline of the RaXPol RHI.

DUNNAVAN ET AL. 5 of 11

RaXPol $K_{\rm dp}$, show decreasing values from 4.0 km toward the surface, likely indicating the presence of aggregates (Dunnavan et al., 2022; Finlon et al., 2022; Kennedy & Rutledge, 2011). Both sets of DWR measurements from the ER-2 aircraft show various regions of enhancements in approximately the same locations as the EXRAD Z, thus also indicating the presence of large aggregates (Barrett et al., 2019).

We explore the use of three state-of-the-art methods that can be used to retrieve D_m in terms of maximum diameter:

1. The X–W DWR empirical third-order polynomial fit from Matrosov et al. (2022) for nadir-pointing radar data (their Figure 6b) applied to the EXRAD and CRS radar data (hereafter, DWR_{X–W} Poly):

$$D_{mv} = 1.31 + 0.146 DWR_{X-W} + 0.0209 DWR_{X-W}^2 - 0.000427 DWR_{X-W}^3.$$
 (1)

In order to convert from D_{mv} to D_m , we follow the same general power-law transformation approach outlined in Matrosov et al. (2022) and derive a power-law fit between each variable from the six ICICLE datasets. The resulting power-law transformation is: $D_m = 0.84 D_{mv}^{0.959}$.

- 2. The Ku–Ka neural network approach developed by Chase et al. (2021) for snow mass-weighted mean diameter applied to the HIWRAP radar data (hereafter, DWR_{Ku-Ka} NN), and
- 3. The empirically optimized Z– $K_{\rm dp}$ bivariate power-law polarimetric retrieval from Dunnavan et al. (2022) (see their Table 1) applied to the RaXPol data (hereafter, RaXPol). We use a spheroidal aspect ratio of $\overline{\omega}=0.25$ and parameter values $\alpha=0.178$ g cm⁻³· mm, and $\sigma=0$ suggested by Figures 12 and 13 in Dunnavan et al. (2022) with $\mu=0$ for simplicity. At RaXPol's wavelength, this results in the bivariate power-law equation:

$$D_{mv,eq} = 0.336 Z_{\rm h}^{1/3} K_{\rm dp}^{-1/3}, \tag{2}$$

where $Z_{\rm h}$ is in linear units of mm⁶ m⁻³ and $D_{mv,\rm eq}$ is D_{mv} in terms of an equivolume diameter. To convert from $D_{mv,\rm eq}$ to D_m (in terms of maximum dimension), we first convert from $D_{mv,\rm eq}$ to D_{mv} with $D_{mv} = \varphi^{-1/3}D_{mv,\rm eq}$. We then convert from D_{mv} to D_m through analytical integration of the assumed gamma PSD. This results in: $D_m = D_{mv}(\mu + \beta_m + 1)/(\mu + 4) = 0.75D_{mv}$, using a mass-dimensional power-law exponent of $\beta_m = 2$ and $\mu = 0$. In order to correctly utilize the third-order polynomial retrieval equation of Matrosov et al. (2022), we only consider retrievals for DWR_{X-W} values between 0 and 20 dB as indicated in their Figures 4 and 6. Retrieved D_m values are only compared at points where valid data exist from all three approaches; a total of 226,545 points met this criterion and were used in the subsequent analysis.

3. Results and Discussion

Figure 4 compares each D_m retrieval method using joint probability density distributions for all eight overpasses as well as the Pearson correlation coefficient (r), bias, and mean absolute error (MAE) for each combination of methods. The highest correlation and lowest bias magnitude and MAE occurred between the two ER-2 DWR retrievals (Figure 4b). Meanwhile, the largest bias magnitude and MAE exists between the RaXPol and DWR_{Ku-Ka} NN D_m estimates, with RaXPol consistently having larger estimates; this discrepancy is aligned with the conclusions of Chase et al. (2021), who report a mean DWR_{Ku-Ka} NN D_m retrieval error of -23% compared to in situ data. Figures 4a and 4c show that the large D_m bias from RaXPol mainly comes from the largest D_m sizes $(6 \text{ mm} \le D_m \le 10 \text{ mm})$. This large bias in RaXPol could result from very low and potentially noisy values of $K_{\rm dp}$ in Equation 2 as shown in Figure 3. The most spread in D_m values exists between RaXPol and DWR_{X-W} Poly D_m , although overall the estimates are not appreciably biased, particularly for smaller (i.e., $D_m < 4 \text{ mm}$) values. In addition, the large variability in RaXPol retrievals compared to the DWR methods could be due to the presence of multiple particle populations of various sizes. While DWR is not directly sensitive to number concentration, the RaXPol polarimetric relation Equation 2, in particular $K_{\rm dp}$, is quite sensitive to number concentration (Dunnavan et al., 2022).

Boxplots of each D_m retrieval method are shown in Figure 4d for each overpass. These results reiterate the statistics from the joint distributions shown in Figures 4a and 4c where DWR_{X-W} Poly and RaXPol median retrievals are universally larger than the DWR_{Ku-Ka} NN retrievals. The DWR_{X-W} Poly and RaXPol distributions agree quite well for early time periods (i.e., 09:26 UTC and 09:50 UTC) but later time periods show more disagreement such as 11:33 UTC and 12:51 UTC where the median D_m values differ by nearly 1 mm. There are also

DUNNAVAN ET AL. 6 of 11

19448007, 2023, 12, Downloaded from https://agupubs.onlinelibrary.wiley.com/doi/10.1029/2023GL103692, Wiley Online Library on [23/07/2023]. See the Terms and Conditions (https://online

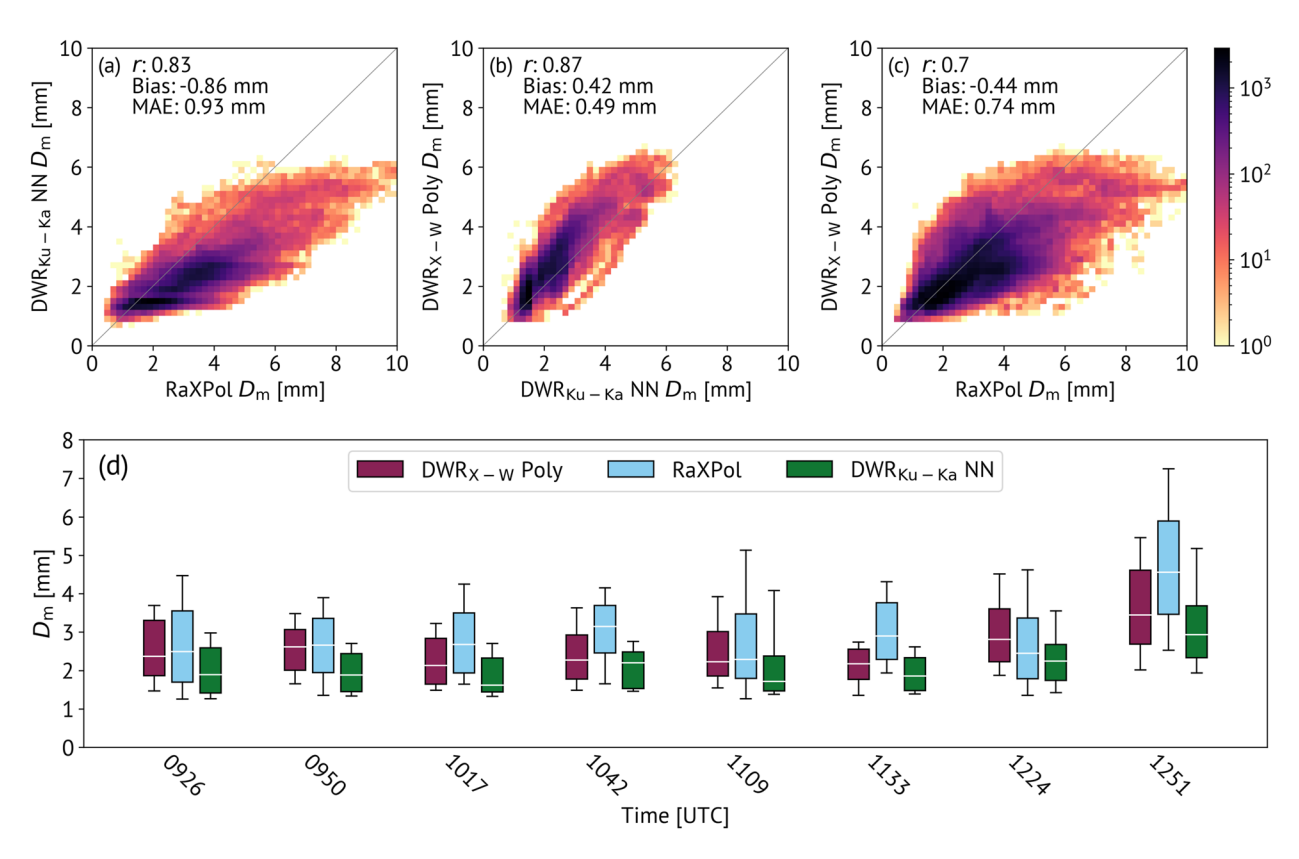


Figure 4. Joint probability density comparison of D_m retrievals for all flyover events for (a) DWR_{X-W} Poly and RaXPol, (b) DWR_{X-W} Poly and DWR_{Ku-Ka} NN, and (c) DWR_{Ku-Ka} NN and RaXPol. Statistics in each subpanel correspond to Pearson correlation coefficient (r), bias (ordinate retrieval minus abscissa retrieval), and mean absolute error (MAE) between each retrieval method. (d) Boxplots of D_m retrievals for each overpass period and retrieval method. Medians are indicated by horizontal white lines, whereas the interquartile range represents the top and bottom of each box. Whiskers represent the 10th to 90th percentiles with outliers excluded.

significant differences between the spread of retrieval values for each method where both DWR_{X-W} Poly and RaXPol exhibit larger interquartile ranges than DWR_{Ku-Ka} NN retrievals for most overpasses. Some overpass periods, such as 12:51 UTC, show interquartile ranges of RaXPol and DWR_{X-W} Poly that are more than twice as large as DWR_{Ku-Ka} NN. While the median retrieved D_m for DWR_{X-W} and RaXPol/DWR_{Ku-Ka} NN stay near 3 and 2 mm for most of the event, respectively, the median values increase for all methods to 3–5 mm by the 12:51 UTC overpass.

Because the ER-2 aircraft has radars with four different frequencies, we are able to generate triple-frequency diagrams for each overpass event. These diagrams illustrate DWR values for two different frequency combinations which can be used to distinguish between various types of particles and microphysical processes such as riming and aggregation (Kneifel et al., 2011, 2015; Kulie et al., 2014; Leinonen & Moisseev, 2015; Leinonen & Szyrmer, 2015; Mason et al., 2019). Figure 5 shows triple-frequency joint probability distributions of DWR_{Ku-Ka} and DWR_{Ka-W} for each overpass period as well as for all overpasses. Overlaid on these joint distributions are discrete dipole approximation scattering simulation results from Leinonen and Moisseev (2015) for synthetic aggregates comprised of plates and needles. Each line corresponds to boundary regions for aggregate distributions characterized by 0.5 mm $\leq D_{mv} \leq$ 8.0 mm and constituent crystal sizes of 0.3, 0.449, 0.716, 0.976, and 1.211 mm.

As shown in Figure 2, the atmosphere was approximately isothermal with $T \approx -5^{\circ}\text{C}$ from 0.5 km MSL to 3.5 km MSL. Therefore, much of the lowest part of the atmosphere was conducive to the growth of plates, columns, and needles (Bailey & Hallett, 2009). For most overpass periods, the scattering simulations of needle aggregates appear to better resemble the observed "hook" shape of the observations. This is best seen for the composite of all overpass periods in Figure 5. However, the joint probability distributions do appear to change from period to period. At early time periods (i.e., 09:26 UTC and 09:50 UTC) both plate and needle aggregates can plausibly explain the observed distributions. Thereafter, needle aggregates better describe the observed hook behavior.

DUNNAVAN ET AL. 7 of 11

1944807, 2023, 12, Downloaded from https://agupubs.onlinelibrary.wiley.com/doi/10.1029/2023GL103692, Wiley Online Library on [23/07/2023]. See the Terms and Conditions (https://onlinelibrary.wiley.com/terms-and-conditions) on Wiley Online Library for rules of use; OA articles are governed

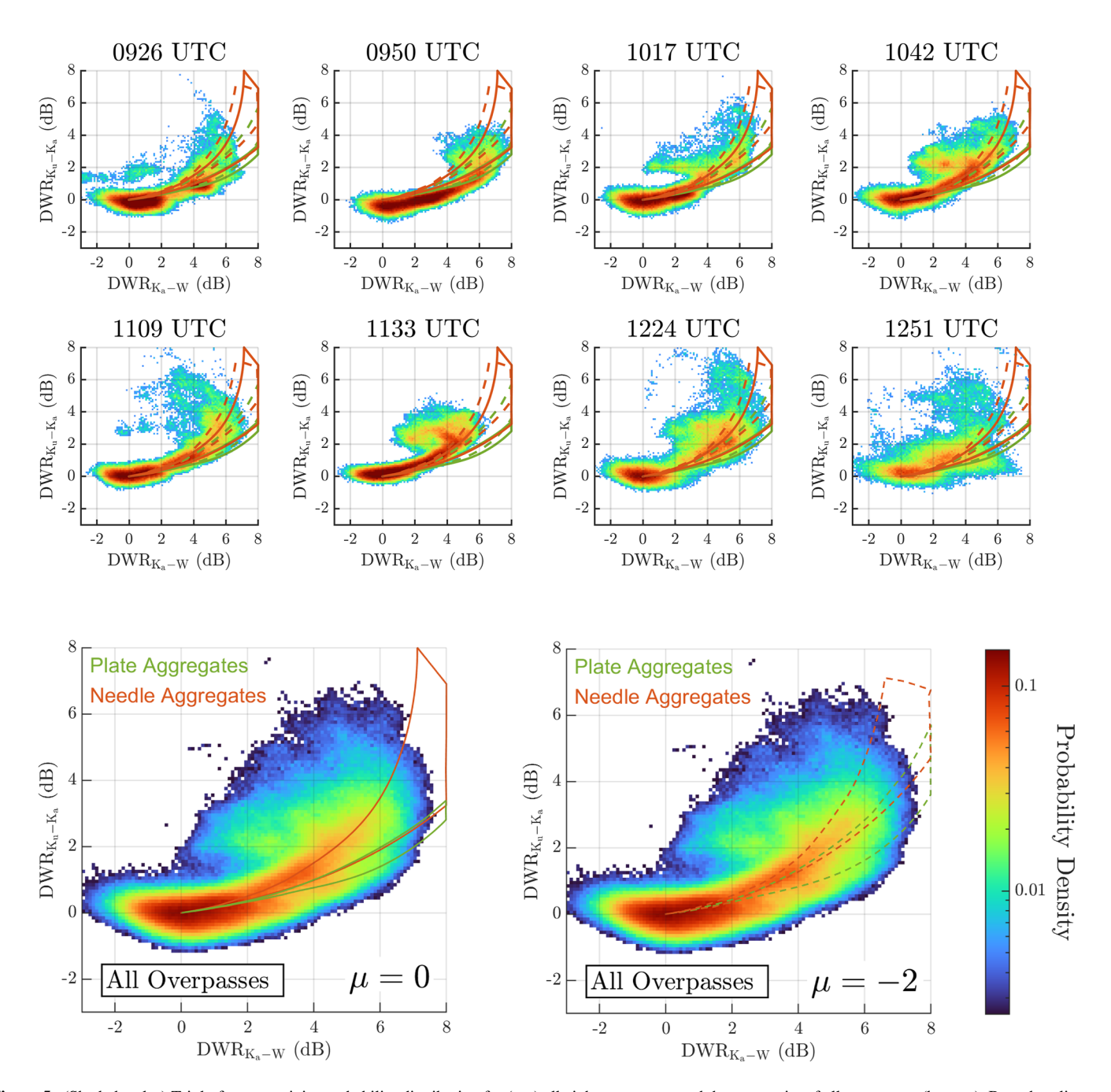


Figure 5. (Shaded, color) Triple-frequency joint probability distribution for (top) all eight overpasses and the composite of all overpasses (bottom). Boundary lines enclose the aggregate scattering database of simulations of Leinonen and Moisseev (2015) for their range of aggregate sizes with constituent crystals that are plates (green) and needles (orange) and $\mu = 0$ (solid, bottom left) or $\mu = -2$ (dashed, bottom right).

Lower values of μ can also better explain the observations. This is best seen for all overpasses where $\mu = -2$ shifts both boundary regions toward lower DWR values for the largest size particles. This impact of μ has been noted in previous studies such as Mason et al. (2019).

By the later times (i.e., 12:24 UTC and 12:51 UTC), there is also a noteworthy increase in spread within the triple-frequency plot coincident with the increase spread in retrieved D_m values from Figure 4. This overall shift could be partially explained by a transition in microphysics where rime splintering and the secondary production of needles could be active at later times. The local increase in supersaturation at lower levels and the increase in low-level MDV and spectral width as shown in Figure 2 could indicate either the local growth of needles and/or

DUNNAVAN ET AL. 8 of 11

9448007, 2023, 12, Downloaded from https:/

riming and the attendant generation of rime splinters. These later time periods could therefore indicate the presence of aggregates composed of needles or splinters. The possibility of needle aggregates is quite important given that each retrieval method was optimized or trained on different data sets. For example, Matrosov et al. (2022) specifically mentions that "it is worth noting that for the ICICLE data set the occurrence of aggregates of needles was quite low." Similarly, the crystals in the IMPACTS 2022 data set in Dunnavan et al. (2022) that was used to optimize the RaXPol D_m retrievals were generally irregular or polycrystalline (see their Figure 6).

4. Summary and Conclusions

In this study, we successfully aligned RHI scans from a ground-based polarimetric radar along the path of concurrent overpasses of nadir-pointing aircraft radars. As shown in Figure 3, the matching of the X-band reflectivities between each platform, when corrected for calibration, was quite accurate and even capable of capturing the same kilometer and even sub-kilometer reflectivity features. Typically, validation and evaluation studies of radar retrievals utilize point measurements (e.g., gauge data or in-situ data) in order to determine some truth for various microphysical variable retrievals such as D_m . While we are not able to utilize these sorts of ground measurements to provide a known truth for our retrieval analysis, we can instead report on the *consistency* of D_m retrieval values from multiple platforms and methodologies as originally proposed. This analysis can therefore be used as a way to report known biases between different retrievals and their mean differences from each other (in terms of MAE).

We found that comparisons of the retrieval methods examined here produced appreciably different estimates of $D_{\rm m}$, with the DWR_{Ku-Ka} NN estimates consistently the smallest and most constrained, and with the RaXPol estimates the least constrained and generally equal to or larger than the DWR_{X-W} Poly estimates. While the signs of these discrepancies were consistent in time, their magnitudes varied. These conclusions rely on the uniqueness of this study and data set, as the resolution and collocation achieved between platforms allowed us to largely alleviate uncertainty in the comparisons due to spatiotemporal differences between methods. Some of the discrepancy between the ER-2 methods could have resulted from undercorrecting W-band attenuation which could artificially inflate DWR_{X-W} and D_m through the Matrosov et al. (2022) polynomial retrieval equation (Equation 1). However, sensitivity tests using larger reported values of $A_{\rm W}$ (not shown) could still not resolve these biases, and the DWR_{Ka-W} shown in Figure 5 agreed well with simulated values, providing some confidence in the employed W-band attenuation correction. Additional uncertainty beyond the originally proposed retrieval methodologies exists due to the additional transformations and assumptions required to achieve a common characteristic size metric (i.e., the mass-weighted mean diameter in terms of particle maximum dimension), as well as assumptions in the computation of $K_{\rm dp}$ (e.g., how much spatial smoothing to employ). In particular, there is uncertainty that results from the assumed mass-dimensional relationship employed for each retrieval.

Triple-frequency plots (Figure 5) provide some indication of the microphysical properties of the snowflakes for each period. Each probability density plot resembles the well-known "hook" shape in DWR_{Ku-Ka}/DWR_{Ka-W} space. Scattering simulations of aggregates based on Leinonen and Moisseev (2015) indicate that both snow aggregates composed of plates and needles can explain each time period. However, most time periods are better represented by needle aggregates rather than plate aggregates. Moreover, $\mu = -2$ values further align the scattering simulations of Leinonen and Moisseev (2015) with the observed values. These simulations suggest that assumptions and particles that were present in the original retrieval studies (Chase et al., 2021; Dunnavan et al., 2022; Matrosov et al., 2022) might not be consistent with the 25 February 2022 IMPACTS IOP aggregates. Scattering simulations of other habits such as dendrite, column, rosette, or spheroid aggregates (not shown) do not better represent the ER-2 measurements than either plate or needle aggregates.

The findings here highlight that, despite progress being made, significant outstanding uncertainties still exist regarding optimizing microphysical remote sensing retrievals of ice quantities. More cases exploring multiple retrieval methods with collocated in situ observations, such as those obtained onboard the accompanying NASA P-3 aircraft during IMPACTS IOPs, will be essential for resolving these uncertainties and discrepancies moving forward.

Data Availability Statement

The 2022 IMPACTS field catalog including the ER-2, RaXPol and ground instrument data is available at http://dx.doi.org/10.5067/IMPACTS/DATA101 (McMurdie et al., 2019). The ICICLE field catalog is publicly available at http://catalog.eol.ucar.edu/icicle. The Neural Network model of Chase et al. (2021) used in this work is

DUNNAVAN ET AL. 9 of 11

19448007, 2023, 12, Downloaded from https://agupubs.onlinelibrary.wiley.com/doi/10.1029/2023GL103692, Wiley Online Library on [23/07/2023]. See the Terms

Acknowledgments

The authors thank Justin Minder and Erin Potter (SUNY Albany) and Leigh Sinclair (University of Alabama at Huntsville) for their help procuring and distributing the MRR-2 data, Randy Chase (Colorado State University) for his help running the Neural Network retrievals, Addison Alford for his manuscript feedback, and the NASA IMPACTS team for their work obtaining the aircraft data. Funding to support this research was provided by NASA IMPACTS Grant 80NSSC19K0399 and by NASA-EP-SCoR Grant 1-511123-OU2-TG. Funding was also provided by NOAA/Office of Oceanic and Atmospheric Research under NOAA-University of Oklahoma Cooperative Agreement NA21OAR4320204, U.S. Department of Commerce. The authors greatly appreciate the comments and suggestions made by the two reviewers of this paper.

available at https://github.com/dopplerchase/Chase_et_al_2021_NN. HRRR model data is available at https://rapidrefresh.noaa.gov/hrrr/. Data for the triple-frequency aggregate scattering simulations of Leinonen and Moisseev (2015) are available in their Supporting Information section.

References

- Bailey, M. P., & Hallett, J. (2009). A comprehensive habit diagram of atmospheric ice crystals: Confirmation from the laboratory, AIRS II, and other field studies. *Journal of the Atmospheric Sciences*, 66(9), 2888–2899. https://doi.org/10.1175/2009JAS2883.1
- Barrett, A. I., Westbrook, C. D., Nicol, J. C., & Stein, T. H. M. (2019). Rapid ice aggregation process revealed through triple-wavelength Doppler spectrum radar analysis. Atmospheric Chemistry and Physics, 19(8), 5753–5769. https://doi.org/10.5194/acp-19-5753-2019
- Benjamin, S. G., Weygandt, S. S., Brown, J. M., Hu, M., Alexander, C. R., Smirnova, T. G., et al. (2016). A North American hourly assimilation and model forecast cycle: The Rapid Refresh. *Monthly Weather Review*, 144(4), 1669–1694. https://doi.org/10.1175/MWR-D-15-0242.1
- Bukovčić, P., Ryzhkov, A. V., & Zrnić, D. (2020). Polarimetric relations for snow estimation Radar verification. Journal of Applied Meteorology and Climatology, 59(5), 991–1009. https://doi.org/10.1175/JAMC-D-19-0140.1
- Bukovčić, P., Ryzhkov, A. V., Zrnić, D., & Zhang, G. (2018). Polarimetric radar relations for quantification of snow based on drisdrometer data. Journal of Applied Meteorology and Climatology, 57(1), 103–120. https://doi.org/10.1175/JAMC-D-17-0090.1
- Chase, R. J., Nesbitt, S. W., & McFarquhar, G. M. (2020). Evaluation of the microphysical assumptions within GPM-DPR using ground-based observations of rain and snow. *Atmosphere*, 11(6), 619. https://doi.org/10.3390/atmos11060619
- observations of rain and snow. *Atmosphere*, 11(6), 619. https://doi.org/10.3390/atmos11060619

 Chase, R. J., Nesbitt, S. W., & McFarquhar, G. M. (2021). A dual-frequency radar retrieval of two parameters of the snowfall particle size distri-
- bution using a neural network. *Journal of Applied Meteorology and Climatology*, 60(3), 341–359. https://doi.org/10.1175/JAMC-D-20-0177.1 Chase, R. J., Nesbitt, S. W., McFarquhar, G. M., Wood, N. B., & Heymsfield, G. M. (2022). Direct comparisons between GPM-DPR and *CloudSat* snowfall retrievals. *Journal of Applied Meteorology and Climatology*, 61(9), 1257–1271. https://doi.org/10.1175/JAMC-D-21-0081.1
- Dias Neto, J., Kneifel, S., Ori, D., Trömel, S., Handwerker, J., Bohn, B., et al. (2019). The TRIple-frequency and Polarimetric radar Experiment for improving process observations of winter precipitation. Earth System Science Data, 11(2), 845–863. https://doi.org/10.5194/essd-11-845-2019
- Dunnavan, E. L., Carlin, J. T., Hu, J., Bukovcic, P., Ryzhkov, A. V., McFarquhar, G. M., et al. (2022). Radar retrieval evaluation and investigation of dendritic growth layer polarimetric signatures in a winter storm. *Journal of Applied Meteorology and Climatology*, 61(11), 1685–1711. https://doi.org/10.1175/JAMC-D-21-0220.1
- Finlon, J. A., McMurdie, L. A., & Chase, R. J. (2022). Investigation of microphysical properties within regions of enhanced dual-frequency ratio during the IMPACTS field campaign. *Journal of the Atmospheric Sciences*, 79(10), 2773–2795. https://doi.org/10.1175/JAS-D-21-0311.1
- Helmus, J. J., & Collis, S. M. (2016). The Python ARM radar toolkit (Py-ART), a library for working with weather radar data in the Python programming language. *Journal of Open Research Software*, 4(1), e25. https://doi.org/10.5334/jors.119
- Heymsfield, G. M., Li, L., & McLinden, M. (2020). ER-2 X-band Doppler Radar (EXRAD) IMPACTS, version 1. NASA Gloal Hydrometeorology Resource Center DAAC. https://doi.org/10.5067/IMPACTS/EXRAD/DATA101
- International Telecommunication Union. (2013). Attenuation by atmospheric gases (Tech. Rep.). International Telecommunication Union Recommendation ITU-R P.676-10. Retrieved from https://www.itu.int/dms_pubrec/itu-r/rec/p/R-REC-P.676-10-201309-S&hx0021;&hx-0021-PDF-F.pdf
- Kennedy, P., & Rutledge, S. (2011). S-band dual-polarization radar observations of winter storms. Journal of Applied Meteorology and Climatology, 50(4), 844–858. https://doi.org/10.1175/2010JAMC2558.1
- Kneifel, S., Kulie, M. S., & Bennartz, R. (2011). A triple-frequency approach to retrieve microphysical snowfall parameters. *Journal of Geophysical Research*, 116(D11), D11203. https://doi.org/10.1029/2010JD015430
- Kneifel, S., von Leber, A., Tiira, J., Moisseev, D., Kollias, P., & Leinonen, J. (2015). Observed relations between snowfall microphysics and triple-frequency radar measurements. *Journal of Geophysical Research: Atmospheres*, 120(12), 6034–6055. https://doi.org/10.1002/2015JD023156
- Kollias, P., Bharadwaj, E., Clothiaux, E. E., Lamer, K., Oue, M., Hardin, J., et al. (2020). The ARM radar network: At the leading edge of cloud and precipitation observations. Bulletin of the American Meteorological Society, 101(5), E588–E607. https://doi.org/10.1175/BAMS-D-18-0288.1
- Kulie, M. S., Hiley, M. J., Bennartz, R., Kneifel, S., & Taneli, S. (2014). Triple-frequency radar reflectivity signatures of snow: Observations and comparisons with theoretical ice particle scattering models. *Journal of Applied Meteorology and Climatology*, 53(4), 1080–1098. https://doi.org/10.1175/JAMC-D-13-066.1
- Kummerow, C., Barnes, W., Kozu, T., Shiue, J., & Simpson, J. (1998). The tropical rainfall measuring mission (TRMM) sensor package. *Journal of Atmospheric and Oceanic Technology*, 15(3), 809–817. https://doi.org/10.1175/1520-0426(1998)015(0809:TTRMMT)2.0.CO;2
- Le, M., & Chandrasekar, V. (2019). Validation of surface snowfall algorithm in GPM dual-frequency precipitation radar. *Journal of Atmospheric and Oceanic Technology*, 36(4), 607–619. https://doi.org/10.1175/JTECH-D-18-0098.1
- Leinonen, J., & Moisseev, D. (2015). What do triple-frequency radar signatures reveal about aggregate snowflakes. *Journal of Geophysical Research: Atmospheres*, 120(1), 229–239. https://doi.org/10.1002/2014JD022072
- Leinonen, J., & Szyrmer, W. (2015). Radar signatures of snowflake riming: A modeling study. Earth and Space Science, 2(8), 346–358. https://doi.org/10.1002/2015EA000102
- Li, L., McLinden, M., & Heymsfield, G. M. (2020). High altitude imaging wind and rain airborne profiler (HIWRAP) IMPACTS, version 1. https://doi.org/10.5067/IMPACTS/HIWRAP/DATA101
- Liao, L., Meneghini, R., Iguchi, T., & Detwiler, A. (1997). Estimation of snow parameters from dual-wavelength airborne radar. In 28th conf. On radar meteorology (pp. 510–511).
- Liao, L., Meneghini, R., Iguchi, T., & Detwiler, A. (2005). Use of dual-wavelength radar for snow parameter estimates. *Journal of Atmospheric and Oceanic Technology*, 10, 1494–1506. https://doi.org/10.1175/JTECH1808.1
- Löffler-Mang, M., & Joss, J. (2000). An optical disdrometer for measuring size and velocity of hydrometeors. *Journal of Atmospheric and Oceanic Technology*, 17(2), 130–139. https://doi.org/10.1175/1520-0426(2000)017(0130:AODFMS)2.0.CO;2
- Löhnert, U., Schween, J. H., Acquistapace, C., Ebell, K., Maahn, M., Barrera-Verdejo, M., et al. (2015). JOYCE: Jülich observatory for cloud evolution. *Bulletin of the American Meteorological Society*, 96(7), 1157–1174. https://doi.org/10.1175/BAMS-D-14-00105.1
- Mason, S. L., Hogan, R. J., Westbrook, C. D., Kneifel, S., Moisseev, D., & von Terzi, L. (2019). The importance of particle size distribution and internal structure for triple-frequency radar retrievals of the morphology of snow. *Atmospheric Measurement Techniques*, 12(9), 4993–5018. https://doi.org/10.5194/amt-12-4993-2019
- Matrosov, S. Y. (1992). Radar reflectivity in snowfall. IEEE Transactions on Geoscience and Remote Sensing, 30(3), 454–461. https://doi.org/10.1109/36.142923

DUNNAVAN ET AL. 10 of 11

- Matrosov, S. Y., Korolev, A., Wolde, M., & Nguyen, C. (2022). Sizing ice hydrometeor populations using the dual-wavelength radar ratio. *Atmospheric Measurement Techniques*, 15(21), 6373–6386. https://doi.org/10.5194/amt-15-6373-2022
- Matrosov, S. Y., Schmitt, C. G., Maahn, M., & de Boer, G. (2017). Atmospheric ice particle shape estimates from polarimetric radar measurements and in situ observations. *Journal of Atmospheric and Oceanic Technology*, 34(12), 2569–2587. https://doi.org/10.1175/JTECH-D-17-0111.1
- McLinden, M., Li, L., & Heymsfield, G. M. (2020). Cloud radar system (CRS) IMPACTS, version 1. NASA Global Hydrometeorology Resource Center DAAC. https://doi.org/10.5067/IMPACTS/CRS/DATA101
- McMurdie, L. A., Heymsfield, G., Yorks, J. E., & Braun, S. (2019). Investigation of microphysics and precipitation for atlantic coast-threatening snowstorms (IMPACTS) collection. NASA EOSDIS Global Hydrology Resource Center Distributed Active Archive Center. https://doi. org/10.5067/IMPACTS/DATA101
- McMurdie, L. A., Heymsfield, G., Yorks, J. E., Braun, S. A., Skofronick-Jackson, G., Rauber, R. M., et al. (2022). Chasing snowstorms: The investigation of microphysics and precipitation for Atlantic coast-threatening snowstorms (IMPACTS) campaign. *Bulletin of the American Meteorological Society*, 103(5), E1243–E1269. https://doi.org/10.1175/BAMS-D-20-0246.1
- Meneghini, R., & Kozu, T. (1990). Spaceborne weather radar. Artech House.
- Murphy, A., Ryzhkov, A., & Zhang, P. (2020). Columnar vertical profile (CVP) methodology for validating polarimetric radar retrievals in ice using in situ aircraft measurements. *Journal of Atmospheric and Oceanic Technology*, 37(9), 1623–1642. https://doi.org/10.1175/jtech-d-20-0011.1
- Myagkov, A., Seifert, P., Bauer-Pfundstein, M., & Wandinger, U. (2016). Cloud radar with hybrid mode towards estimation of shape and orientation of ice crystals. *Atmospheric Measurement Techniques*, 9(2), 469–489. https://doi.org/10.5194/amt-9-469-2016
- National Centre for Atmospheric Science. (2023). Chilbolton atmospheric observatory (CAO). Retrieved from https://amof.ac.uk/observatory/chilbolton-atmospheric-observatory-cao/
- Nguyen, C. M., Wolde, M., Battaglia, A., Nichman, L., Bliankinshtein, N., Haimov, S., et al. (2022). Coincident in situ and triple-frequency radar airborne observations in the Arctic. Atmospheric Measurement Techniques, 15(3), 775–795. https://doi.org/10.5194/amt-15-775-2022
- Pazmany, A. L., Mead, J. B., Bluestein, H. B., Synder, J. C., & Houser, J. B. (2013). A mobile rapid-scanning X-band polarimetric (RaXPol) Doppler radar system. *Journal of Atmospheric and Oceanic Technology*, 30(7), 1398–1413. https://doi.org/10.1175/JTECH-D-12-00166.1
- Petäjä, T., O'Conner, E. J., Moisseev, J., Sinclair, D., Manninen, V. A., Väänänen, R., et al. (2016). BAECC: A field campaign to elucidate the impact of biogenic aerosols on clouds and climate. Bulletin of the American Meteorological Society, 97(10), 1909–1928. https://doi. org/10.1175/BAMS-D-14-00199.1
- Protat, A., Rauniyar, S., Delanoë, J., Fontaine, E., & Schwarzenboeck, A. (2019). W-band (95 GHz) radar attenuation in tropical stratiform ice anvils. *Journal of Atmospheric and Oceanic Technology*, 36(8), 1463–1476. https://doi.org/10.1175/jtech-d-18-0154.1
- Ryzhkov, A. V., & Zrnić, D. S. (2019). Radar polarimetry for weather observations. Springer Atmospheric Sciences.
- Ryzhkov, A. V., Zrnic, D. S., & Gordon, B. A. (1998). Polarimetric method for ice water content determination. *Journal of Applied Meteorology and Climatology*, 37(2), 125–134. https://doi.org/10.1175/1520-0450(1998)037(0125;PMFIWC)2.0.CO:2
- Schrom, R. S., & Kumjian, M. R. (2016). Connecting microphysical processes in Colorado winter storms with vertical profiles of radar observations. *Journal of Applied Meteorology and Climatology*, 55(8), 1771–1787. https://doi.org/10.1175/JAMC-D-15-0338.1
- Schvartzman, D., Torres, S. M., & Warde, D. (2020). The hybrid-scan estimators: Exploiting WSR-88D split cuts to improve the quality of polarimetric-variable estimates. *Journal of Atmospheric and Oceanic Technology*, 37(2), 299–315. https://doi.org/10.1175/jtech-d-19-0071.1
- Skofronick-Jackson, G., Kulie, M., Milani, L., Munchak, S. J., Wood, N. B., & Levizzani, V. (2019). Satellite estimation of falling snow: A global precipitation measurement (GPM) Core observatory perspective. Journal of Applied Meteorology and Climatology, 58(7), 1429–1448. https://doi.org/10.1175/JAMC-D-18-0124.1
- Tridon, F., Gattaglia, A., Chase, R. J., Turk, F. J., Leinonen, J., Kneifel, S., et al. (2019). The microphysics of stratiform precipitation during OLYMPEX: Compatibility between triple-frequency radar and airborne in situ observations. *Journal of Geophysical Research: Atmospheres*, 124(15), 8764–8792. https://doi.org/10.1029/2018JD029858
- Vulpiani, G., Baldini, L., & Roberto, N. (2015). Characterization of mediterranean hail-bearing storms using an operational polarimetric X-band radar. Atmospheric Measurement Techniques. 8(11), 4681–4698. https://doi.org/10.5194/amt-8-4681-2015
- Vulpiani, G., Montopoli, M., Passeri, L. D., Gioia, A. G., Giordano, P., & Marzano, F. S. (2012). On the use of dual-polarized C-band radar for operational rainfall retrieval in mountainous areas. *Journal of Applied Meteorology and Climatology*, 51(2), 405–425. https://doi.org/10.1175/JAMC-D-10-05024.1
- Zrnić, D. S., & Ryzhkov, A. V. (1999). Polarimetry for weather surveillance radars. Bulletin of the American Meteorological Society, 80(3), 389–406. https://doi.org/10.1175/1520-0477(1999)080(0389:PFWSR)2.0.CO;2

DUNNAVAN ET AL. 11 of 11